Three-phase tri-state buck–boost integrated inverter for solar applications

Moacyr de Brito[1] ✉, Leonardo Sampaio[2], Guilherme Melo[3], Carlos Alberto Canesin[3]

[1]Department of Electronic Engineering – DAELN, Federal Technological University of Paraná, Via Rosalina Maria dos Santos,
1233 Campo Mourão, PR, Brazil
[2]Department of Electric Engineering, Federal Technological University of Paraná, Avenida Alberto Carazzai, 1640 Cornélio Procópio,
PR, Brazil
[3]Department of Electric Engineering, São Paulo State University, Av. Prof. José Carlos Rossi, 1370 Ilha Solteira, SP, Brazil
✉ E-mail: moa.brito@gmail.com

Abstract: This study presents a three-phase tri-state buck–boost integrated inverter suitable for stand-alone and/or grid-connected photovoltaic (PV) energy applications. The usage of the special features of the tri-state operation coupled with a modified space vector modulation allows the inverter to present a remarkable degree of freedom for the controllers' design, that is, input and output can be independently controlled. As the input can be autonomously controlled, this converter is very attractive for interfacing renewable energy sources as PV panels, once the main duty cycle D_1 controls the maximum power point tracking and the second duty cycle D_2 is responsible to feed the output. It should be pointed out that there are no power electrolytic capacitors in this integrated inverter, which results in a major advantage for the structure working life and it is the first time in the literature that this inverter is used to feed power into the grid. Throughout this study the system is described, the modulation and control schemes are presented and interesting experimental results are available in order to confirm the outstanding features of this proposal.

1 Introduction

The research and improvement of new power electronics inverters are mandatory to improve the viability of distributed generation through renewable energy sources usage [1, 2]. In this context, the power electronics plays a fundamental role and, usually, photovoltaic (PV) energy sources provide low DC voltage that needs voltage boost, a good input maximum power point tracking (MPPT) [3–5], and low total harmonic distortion (THD) for the output AC voltage/current. These criteria may be economically determinant in the future use of renewable energies such as wind and solar once the most expected applications with renewable sources are the grid-tied or grid-connected, where no local energy storage is needed and all benefits of distributed generations could be achieved.

The tri-state inverters have been shown as promising structures related to their dynamic performance, efficiency and lifetime. As current-source inverter (CSI), it presents implicit short-circuit protection, ruggedness and direct current control ability that permits to feed capacitive and/or low impedances with ease [6, 7].

In this context, this paper presents the three-phase tri-state buck–boost inverter with independent input to output control through D_1 and D_2 duty cycles, a modified space vector modulation (SVM) and $dq0$ transformation for the control scheme allowing exceptionally high-quality performance for the entire system control. Moreover, experimental evaluations of a PV grid-tied inverter are shown in order to demonstrate the feasibility of the proposal.
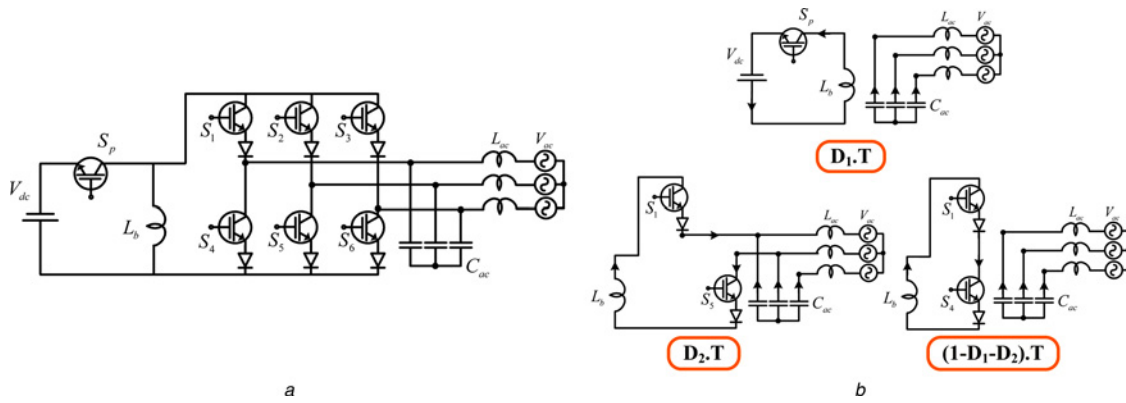
2 Proposed three-phase tri-state inverter

The proposed system, as depicted in Fig. 1*a*, consists of a three-phase tri-state integrated buck–boost inverter with CL filter for grid-tied mode, whereas on stand-alone mode only C filter is mandatory. Note that it is not necessary to add a diode in series with S_p switch because it is not necessary to block reverse voltages as was not done in [7].

This inverter presents three important states, namely short-circuit, active and free-wheeling states. The short-circuit state charges the buck–boost inductor, the active state is responsible for feeding the output, whereas the free-wheeling state works for maintaining the energy stored. The short-circuit time occurs during $D_1.T$, the active state occurs for $D_2.T$ and the free-wheeling state lasts during $(1–D_1–D_2).T$, as shown in Fig. 1*b*. T is the switching period, and the operation modes are based on continuous conduction mode.

The tri-state operation is capable of improving the dynamic performance, reducing the right half-plane zero effects, typical in conventional boost converters in voltage mode control [6–9] and besides this converter has the advantage of increasing the static gain. In the literature $D_2.T$ time interval is always made fixed but it is also possible to make both $D_1.T$ and $D_2.T$ time intervals varying. This characteristic makes this operation even more attractive, allowing the input to output power decoupling for single-phase systems eliminating the pulsed power at twice the grid frequency [10]. In this paper, these attributes are used at the modulation and control scheme of the proposed tri-state buck–boost three-phase inverter. However, in a different manner, as the three-phase power is constant it is not necessary to have a power decoupling but input and output can be controlled independently. This feature allows this converter to be suitable for interfacing renewable energy sources as the input MPPT and output current injection with reduced THD can be performed independently. Thus making this application entirely diverse from [7]. Another advantage of this three-phase system is that all storage elements are reduced compared with its single-phase counterpart [10], meaning lifetime improvements. It is necessary to emphasise that it is the first time in the literature that this inverter is used to inject power into the grid.

3 Modified space vector modulation

The SVM is fairly used in three-phase inverters because of its special features as better exploitation of DC link, low THD for the output voltage/currents and less switching losses [11–14]. Basically, it considers a voltage vector that can be inserted into a six sector

Fig. 1 *Proposed three-phase tri-state inverter*

a Proposed three-phase tri-state inverter in grid-tied mode
b Operation modes of the proposed buck–boost inverter, considering the switching of S_P, S_1, S_4 and S_5 as example
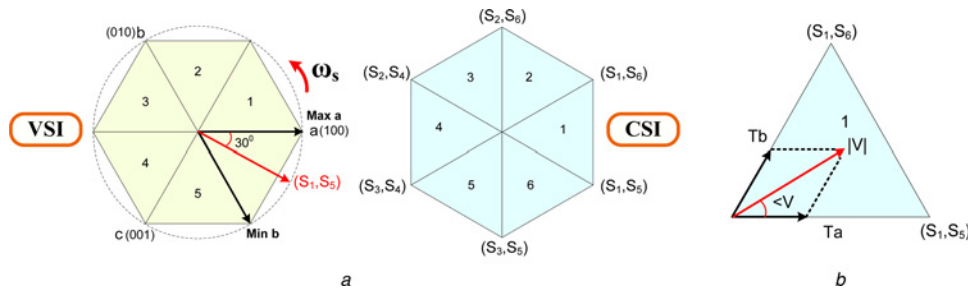
Fig. 2 *Modified SVM*

a VSI and CSI SVM
b Projection calculus based on sector 1

hexagon to determine the switching states. Using the conventional SVM for voltage-source inverters (VSIs), it is possible to determine the space vectors for CSIs. Fig. 2*a* shows the achievement of CSI SVM from VSI SVM.

The CSI sectors are lagged 30° from VSI sectors. Another interesting feature is that differently from VSI in which three switches are always in conduction, at CSIs only two switches must be conducting in the same time interval. It is mandatory once the AC side is mainly capacitive and thus it must not be short-circuited and because the DC bus is of the current-source type it cannot be opened. These both constraints are performed once only one top switch and only one bottom switch are gated simultaneously.

The next step is the calculus of the projections based on the sector. Assuming the rotation of 30°, it is possible to use only sector 1, considered in phase with phase *a*, that is, phase *a* is 0°, for this

calculus as shown in Fig. 2*b*. In this space vector approach, all vectors will be sent to sector 1.

Equations (1)–(3) determine the switching times T_a, T_b and T_{null}. T_{null} represents the free-wheeling time and T_a plus T_b represents D_2 time

$$T_a = |V|.\left(\cos \angle(V) - (\sqrt{3}/3)\sin \angle(V)\right) \quad (1)$$

$$T_b = |V|.\left((2\sqrt{3}/3)\sin \angle(V)\right) \quad (2)$$

$$T_{null} = T_s - T_a - T_b \quad (3)$$

Differently from the conventional modulator, this tri-state presents an additional D_1 varying control time, and which is inserted into
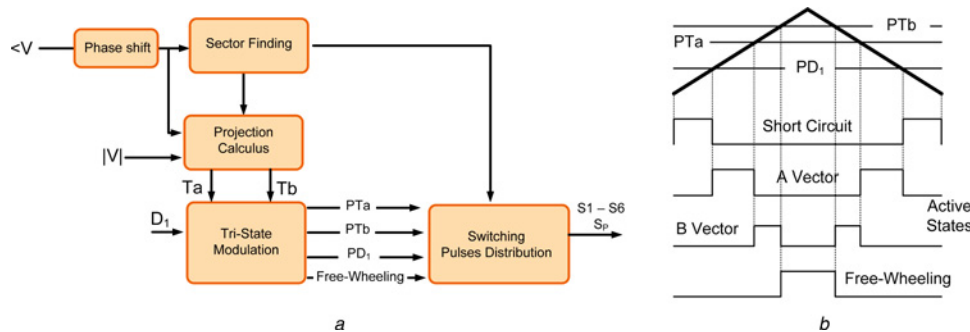
Fig. 3 *Entire block diagram of the proposed SVM*

a Block diagram of the novel CSI SVM
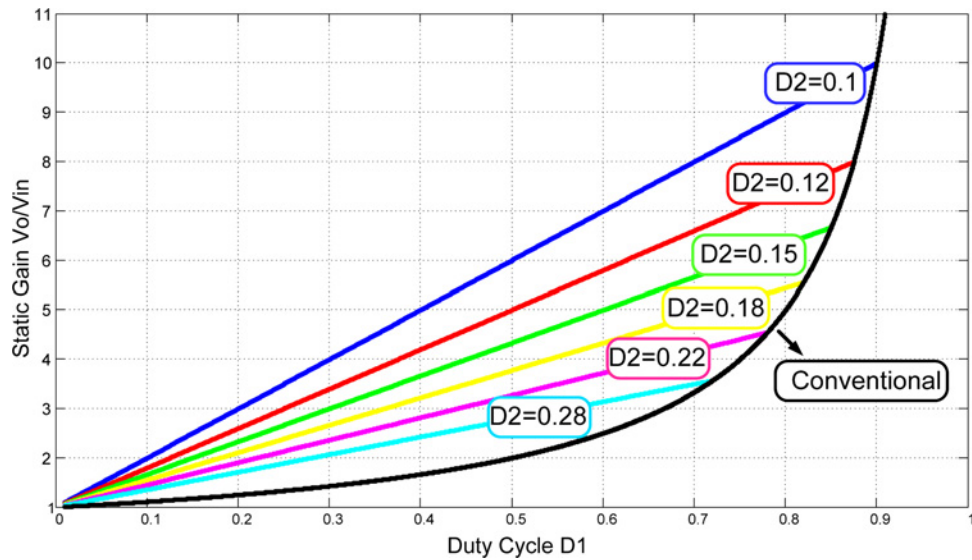*b* Possibility for implementing the tri-state modulation

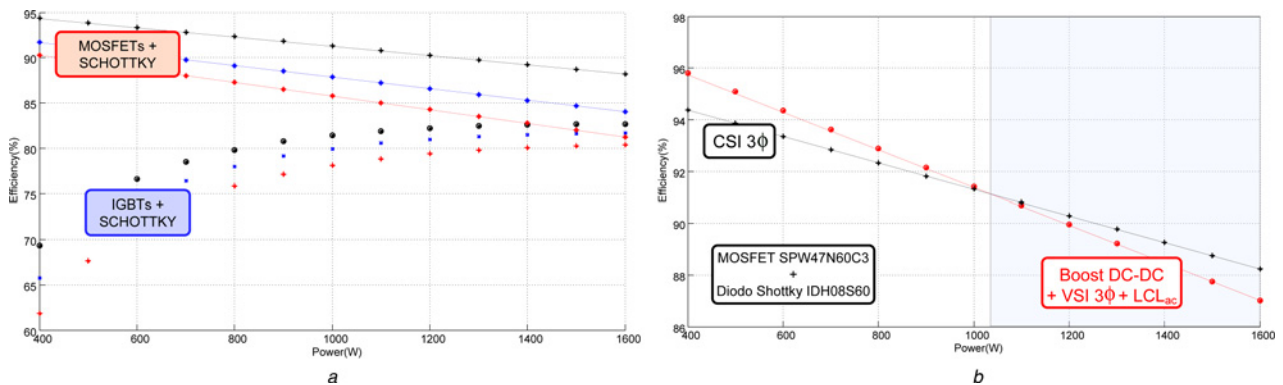**Fig. 4** *Static gain for different scenarios*

Fig. 5 *Converter total losses*

a CSI efficiency for different semiconductors scenarios
b Efficiency for the tri-state three-phase buck–boost inverter and VSI + LCL$_{ac}$ + boost DC–DC with the best semiconductor option

the tri-state CSI SVM, and because of that (1)–(3) are scaled based on D_1 size to maintain the proper modulation characteristics, and the total time are assumed to be equal to one (per unit).

The entire block diagram of the proposed SVM is shown in Fig. 3*a*, and one manner for implementing this modulation is also observed at Fig. 3*b*.

4 Mathematical analysis

The converter state-space average model including inductor losses is presented in (4) based on the topological states of Fig. 2*b*. L_B represents the inductance of the buck–boost inductor, R_{LB} is the resistance of the inductor, C_o is the equivalent output capacitance,

V_{in} is the input voltage and I_o is the output current formed by the output inductance and the grid. V_o represents the line output voltage and its maximum value reflects in the DC bus of the converter

$$
\begin{bmatrix} \dot{I}_{LB} \\ \dot{V}_o \end{bmatrix} = \begin{bmatrix} -R_{LB}/L_B & -D_2/L_B \\ D_2/C_o & 0 \end{bmatrix} \cdot \begin{bmatrix} I_{LB} \\ V_o \end{bmatrix}
$$
$$
+ \begin{bmatrix} (D_1 + D_2)/L_B & 0 \\ 0 & -1/C_o \end{bmatrix} \cdot \begin{bmatrix} V_{in} \\ I_o \end{bmatrix} \tag{4}
$$

From this set of equations, it is possible to obtain the static gain G, where one can verify that the static gain is a function of two

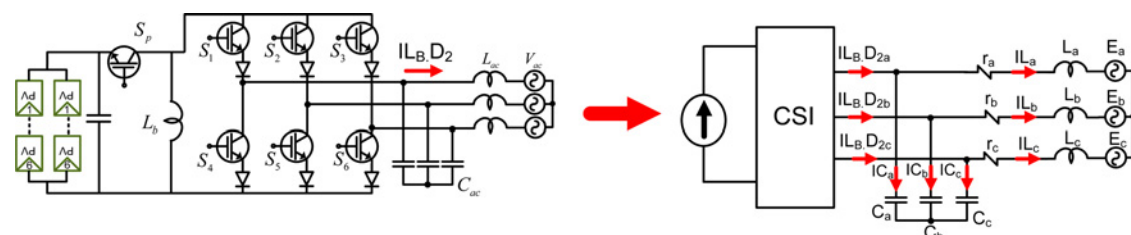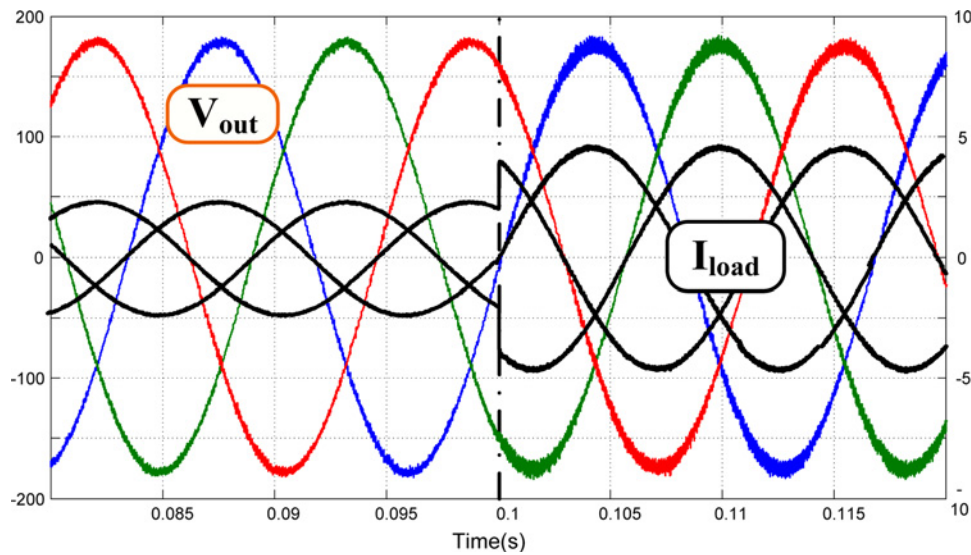**Fig. 6** *Equivalent circuit for controlling the converter's output*

Fig. 7 *Output voltages and output currents during transient*
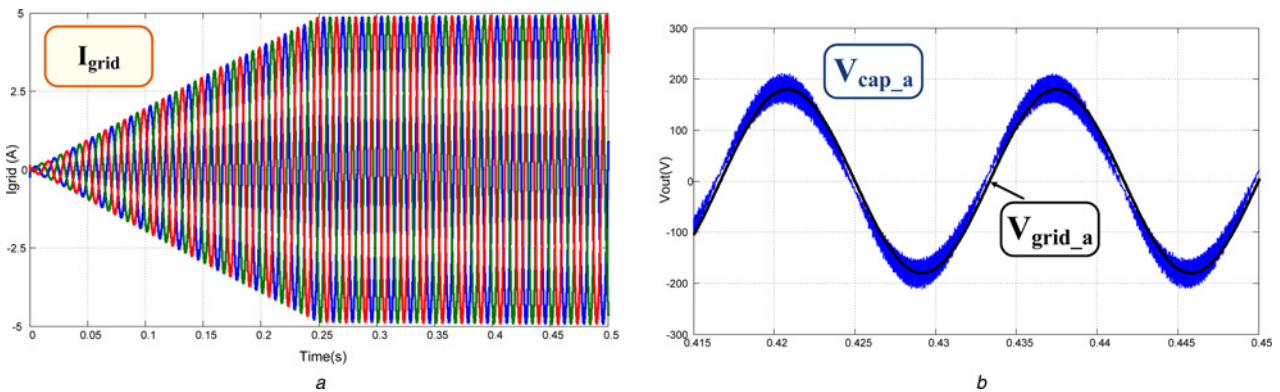

Fig. 8 *Injected grid currents*
a Three-phase injected grid currents
b Phase displacement between V_{cap} and V_{grid} for phase *a*

distinct duty cycles D_1 and D_2, considering R_o (V_o/I_o) as an equivalent load

$$G = V_o/V_{in} = \frac{D_1}{D_2 + (R_{LB}/R_o).(1/D_2)} \qquad (5)$$

Only for comparison criteria, the static gain graph for this tri-state buck–boost integrated inverter and for the conventional three-phase buck–boost inverter are presented in Fig. 4. Considering the inductor losses reduced close to zero, one can verify that the proposed converter has an increased static gain (linear lines). Another interesting evaluation is regarded the converter total losses and they were evaluated and plotted in Fig. 5a, for different types of semiconductors. The losses in the electromagnetic elements are also included. The best option, considering the current technologies, is the usage of MOSFET plus Schottky diodes. The same comparison is done with the conventional three-phase VSI inverter with the DC–DC boost converter in cascade, once this approach is the most used with low/medium power and low input voltage where voltage boost is necessary to permit injection of power to the grid. This VSI converter presents an LCL output filter. From Fig. 5b, it is possible to verify that the tri-state inverter is very attractive for power in the range over 1 kW, considering V_{in} at 100 V. The losses considering sensors/actuators and auxiliary power source are neglected.

Table 1 PV module electrical parameters

Maximum power	P_{max} = 189 Wp
Voltage at MPP	V_{MPP} = 25.1 V
Current at MPP	I_{MPP} = 7.55 A
Open-circuit voltage	V_{oc} = 32.9 V
Short-circuit current	I_{sc} = 8.21 A
Temperature coefficient of I_{sc}	α = 3.18 × 10^{-3} A/°C

5 Inverter control schemes

The three-phase tri-state inverter control is based on $dq0$ transformation [15–17]. A three-phase set of variables can be transformed into DC quantities using this approach, making the control scheme very attractive. Thus, all three-phase variables are reduced to sets of two sensed variables for the input control. The example in this section is based on grid-tied mode.

The control of the input current is performed independently from the injected grid current by the MPPT algorithm and this control gives $D_1.T$ time interval. The output control is done with the second duty cycle D_2 and represents the time interval of the adjacent space vectors ($D_2.T$). The injected grid current and its reference are obtained through Park and Clark transformations ($dq0$). The obtainment of matrix T (*abc* to $dq0$) is shown in Appendix 2. This control is divided into three steps, namely output grid current control, feedforward control and output capacitors control. The output grid current control (grid power)
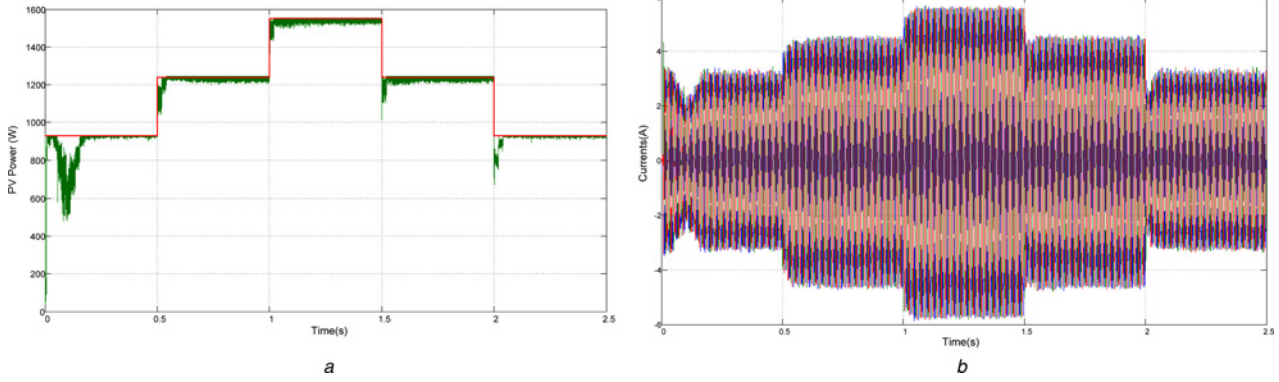
Fig. 9 *Injected grid currents and the power drained from the PV source*
a Power extracted from PV source from a variable power profile
b Grid-injected currents

gives the reference for the output capacitors control that has the feedforward control to guarantee the effectiveness of the proposed scheme. The feedforward control maintains null output current when no current reference is necessary, that is, it reproduces the grid voltages at the output capacitors. Finally, the capacitors control gives the $D_2.T$ time interval for the modulator. For working in stand-alone mode, the control system is reduced and blocks concerning the output grid control and phase locked loop (PLL) can be removed.

The output control (current plus voltage control) is performed in accordance with (8) and (11) that were obtained applying $dq0$ transformation in the output grid currents and in the output capacitors voltages. The equivalent circuit for this calculus is depicted in Fig. 6. All elements were considered with the same parameters. When applying this transformation, the direct axis (d-axis) is cross-coupled with the quadrature axis (q-axis) and the decoupling scheme is applied to overcome this issue, that is, direct feed of E_q, E_d, $\omega.L.IL_q$ and $\omega.L.IL_d$ at (8).

Applying Kirchhoff's voltage law one can find (6). Applying $dq0$ transformation (matrix T) one can find (7)

After algebraic manipulations, (8) represents the current control

$$\begin{cases} r.IL_d + L\dfrac{d\,IL_d}{dt} = VC_d + \omega.L.IL_q - E_d \\ r.IL_q + L\dfrac{d\,IL_q}{dt} = VC_q - \omega.L.IL_d - E_q \end{cases} \quad (8)$$
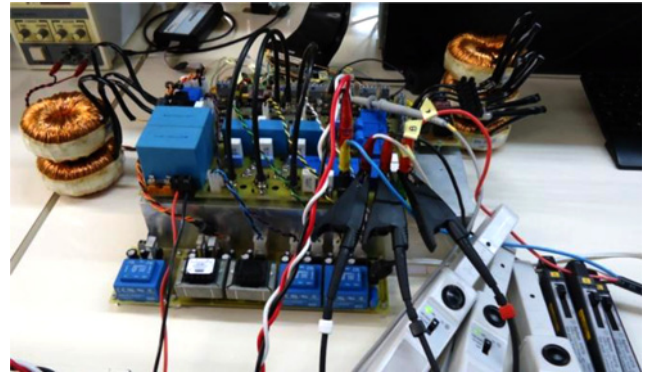
Applying Kirchhoff's current law one can find (9). Applying $dq0$ transformation (matrix T) one can find (9)

$$\begin{bmatrix} IL_a \\ IL_b \\ IL_c \end{bmatrix} = \begin{bmatrix} IL_b.d_{2a} \\ IL_b.d_{2b} \\ IL_c.d_{2c} \end{bmatrix} - \begin{bmatrix} C_a & 0 & 0 \\ 0 & C_b & 0 \\ 0 & 0 & C_c \end{bmatrix}\dfrac{d}{dt}\begin{bmatrix} VC_a \\ VC_b \\ VC_c \end{bmatrix} \quad (9)$$

Fig. 10 *Three-phase tri-state prototype*

After algebraic manipulations, (11) represents the voltage control
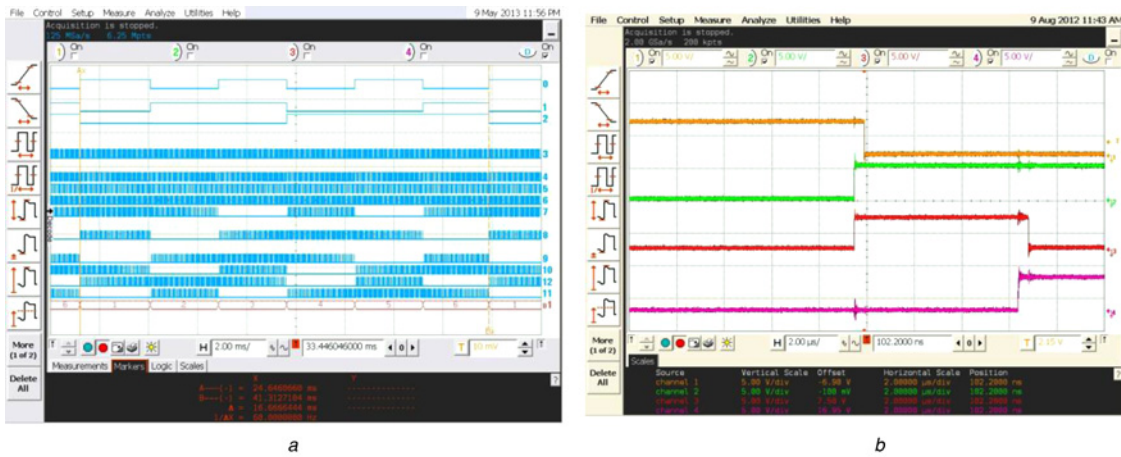
$$\begin{cases} C.\dfrac{d\,VC_d}{dt} = \omega.C.VC_q - IL_b.d_{2d} - IL_d \\ C.\dfrac{d\,VC_q}{dt} = -\omega.C.VC_d - IL_b.d_{2q} - IL_q \end{cases} \quad (11)$$

6 Simulation results

The simulations are developed using MATLAB/SIMULINK® platform. The main simulation parameters are: $V_{in} = 100$ V; $L_b = 5$ mH; $C_{ac} = 8.2$ μF; $L_{ac} = 3$ mH and $P_{out} = 1.3$ kW at $127\ V_{rms}$.

First, for stand-alone mode, the output voltages and output currents are shown in Fig. 7, describing a load step change.

For grid-connected mode, the injected grid currents are shown in Fig. 8*a* and the capacitor voltage of phase 'a' is shown in Fig. 8*b*

$$\begin{cases} \begin{bmatrix} VC_a \\ VC_b \\ VC_c \end{bmatrix} = \begin{bmatrix} r_a & 0 & 0 \\ 0 & r_b & 0 \\ 0 & 0 & r_c \end{bmatrix}\begin{bmatrix} IL_a \\ IL_b \\ IL_c \end{bmatrix} + \begin{bmatrix} L_a & 0 & 0 \\ 0 & L_b & 0 \\ 0 & 0 & L_c \end{bmatrix}\dfrac{d}{dt}\begin{bmatrix} IL_a \\ IL_b \\ IL_c \end{bmatrix} + \begin{bmatrix} E_a \\ E_b \\ E_c \end{bmatrix} \end{cases} \quad (6)$$

$$\begin{cases} \begin{bmatrix} VC_d \\ VC_q \\ VC_0 \end{bmatrix} = \begin{bmatrix} r & 0 & 0 \\ 0 & r & 0 \\ 0 & 0 & r \end{bmatrix}\begin{bmatrix} IL_d \\ IL_q \\ IL_0 \end{bmatrix} + \begin{bmatrix} L & 0 & 0 \\ 0 & L & 0 \\ 0 & 0 & L \end{bmatrix}\left(T.\dfrac{dT^{-1}}{dt}\begin{bmatrix} IL_d \\ IL_q \\ IL_0 \end{bmatrix} + T.T^{-1}.\dfrac{d}{dt}\begin{bmatrix} IL_d \\ IL_q \\ IL_0 \end{bmatrix}\right) + \begin{bmatrix} E_d \\ E_q \\ E_0 \end{bmatrix} \end{cases} \quad (7)$$

$$\begin{cases} \begin{bmatrix} IL_d \\ IL_q \\ IL_0 \end{bmatrix} = \begin{bmatrix} IL_b.d_{2d} \\ IL_b.d_{2q} \\ IL_c.d_{20} \end{bmatrix} - \begin{bmatrix} C & 0 & 0 \\ 0 & C & 0 \\ 0 & 0 & C \end{bmatrix}\left(T.\dfrac{dT^{-1}}{dt}\begin{bmatrix} VC_d \\ VC_q \\ VC_0 \end{bmatrix} + T.T^{-1}.\dfrac{d}{dt}\begin{bmatrix} VC_d \\ VC_q \\ VC_0 \end{bmatrix}\right) \end{cases} \quad (10)$$

Fig. 11 *Signals that compound the SVM scheme*

a All pulses for the obtainment of the SVM-CSI
b Short-time among pulse transitions
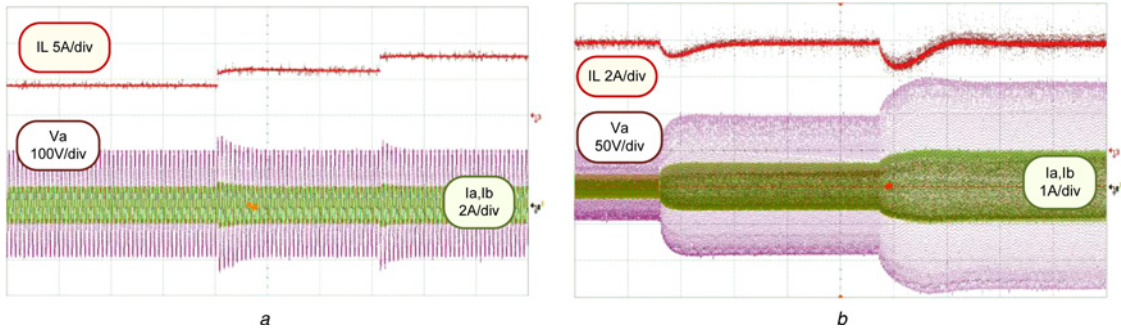
Fig. 12 *Input to output decoupling*

a Current steps applied at buck–boost inductor. Red (Upper): current through the buck–boost inductor; purple (below grey): output voltage at phase 'a'; and green (below black): current at phases 'a' and 'b'. Time: 200 ms/div
b Voltage steps at the converter's output. Red (Upper): current through the buck–boost inductor; purple (below grey): output voltage at phase 'a'; and green (below black): current at phases 'a' and 'b'. Time: 500 ms/div
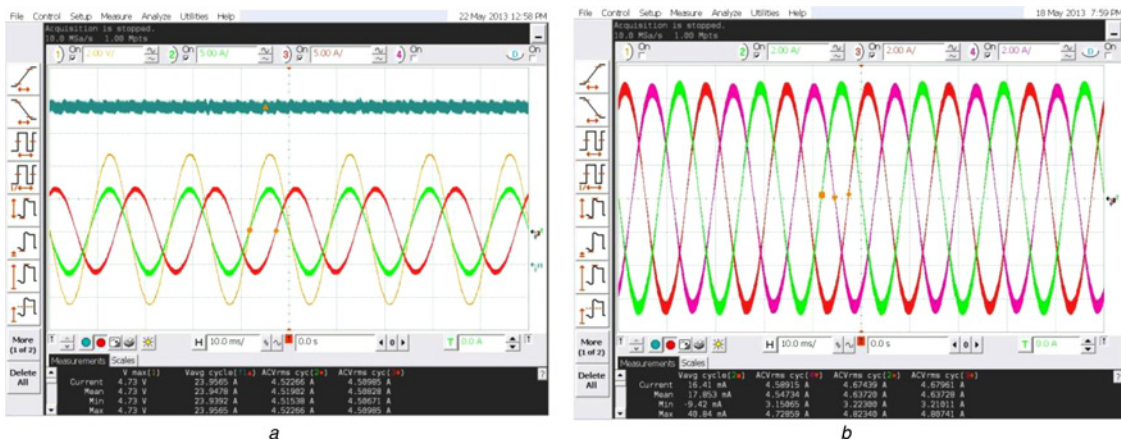

Fig. 13 *Main experimental results*

a Current through the buck–boost inductor and voltage at phase 'a' together with currents through phases 'a' and 'b'. Cyan (Upper): current through buck–boost inductor; yellow (below thin grey): voltage at phase 'a'; green (below thick grey): current at phase 'a'; and red (below thick black): current at phase 'b'. Time: 20 ms/div
b Three-phase injected grid currents. Time: 20 ms/div

together with the grid voltage for demonstrating the phase displacement angle for the active power transfer.

The constant voltage source was replaced by a PV model (PV source) and the main PV electrical parameters are summarised in Table 1, for one PV module. The PV association is based on a four series connected PV modules in two parallel branches,

representing 8 PV panels (1.5 kW$_{peak}$). The injected grid currents and the power drained from the PV source can be visualised at Fig. 9 with a varying power profile. Such results were obtained with P&O algorithm. Thus, $D_1.T$ time interval is obtained directly from the MPPT algorithm. The tracking factor, percentage of available energy that could be extracted, reaches almost 98% in
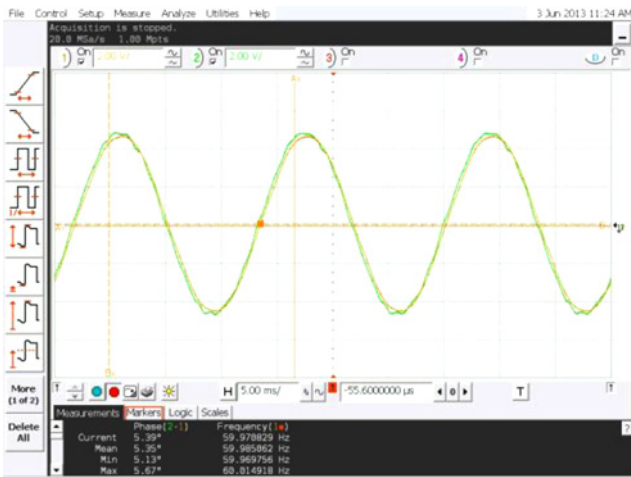
Fig. 14 *Voltages of the output capacitor and grid for phase 'a' – active power injection. Time: 5 ms/div*

this situation. However, any other MPPT method can be applied and different tracking factors can be found depending on the used power profile [5].

As one can verify from the simulation results, this converter can be very useful for three-phase grid-tied PV inverters with low/medium power and low input voltage.

7 Experimental results

The prototype shown in Fig. 10 was built in laboratory and the initial tests were done regarding its modulation scheme, input to output independently control while feeding a stand-alone three-phase load. The converter was built according to the specifications of Section 6. As one can see, there are no power electrolytic capacitors in this integrated inverter. The SPW47N60 MOSFETs and SCS108AG SiC Schottky diodes were used.

At Fig. 11a, it is possible to verify all the signals that compound the SVM scheme. Pulses 0–2 represent the SVM sectors (i.e. 1–6). Pulses 3–5 represent the time of the D_1 pulse and the time of the adjacent space vectors T_a and T_b. Pulses 6–12 represent the switching drives.

As one can verify, it is shown the decoded BUS sector demonstrating that the modulation is applied correctly once the BUS moves repeatedly from 1–6 in sequence. Finally, differently from VSI inverters it is necessary to implement short-circuits

between pulse transitions in order to prevent the inverter from damages, what is demonstrated easily from Fig. 11b.

At Fig. 12, it is possible to verify the input to output decoupling. Fig. 12a shows current steps at the input (current through the buck–boost inductor), whereas the outputs (three-phase voltages and currents) remain constant. Moreover, Fig. 12b demonstrates the same proposal but the steps are applied at the outputs while the current through the inductor is maintained constant. The verified under/overshoots are regarded the time constants of the compensators. These experimental results prove that D_1 and D_2 duty cycles can control independently the input and the output of the power inverter, simplifying the system control. Obviously that when in operation an increase of power at the input will represent an increase of power at the output in order to maintain maximum efficiency and to reduce the reactive circulation inside the power inverter. All voltages are measured from line to neutral and the currents are measured as positive when going out from the inverter (stand-alone) and as positive when injected to the grid (grid-connected).

Fig. 13a shows the current over the input inductor and the output voltage at phase 'a' together with the output currents of phases 'a' and 'b'. The resistive local load is about 28 Ω in star configuration performing almost 1750 W at the output. Moreover at Fig. 13b it is possible to verify all three-phase output currents for the same load condition.

Before connecting the power inverter to the grid, it is extremely necessary to synchronise both grid and inverter. This was done reproducing the instantaneous grid voltages over the output AC capacitors in such manner that at the moment of connection no power flux between inverter and grid was observed. Moreover, it minimises possible oscillations among systems minimising operational problems for the inverter and for loads attached to the grid.

After attachment it is necessary to start the active power transfer via phase angle varying. This is shown in Fig. 14 where one can easily verify the inverter and grid voltage phase angle for phase 'a'.

Fig. 15a shows the voltage over phase 'a' together with the current at the local load and the current being injected to the grid. The power current probes are connected to exhibit positive current when inverter feed power to the grid. Finally, Fig. 15b shows the voltage over phase 'a' together with the three-phase low-harmonic injected grid currents. The total current harmonic distortion is about 2.9%, considering Fluke 435II measurement system.

Another interesting feature of this inverter is that it presents the inherent boost characteristic eliminating the cascaded DC–DC front converter to boost the input voltage. Moreover, for low-to-intermediate power levels the association of PV panels cannot provide the necessary voltage to connect directly a VSI inverter making this CSI tri-state three-phase inverter very

a

b
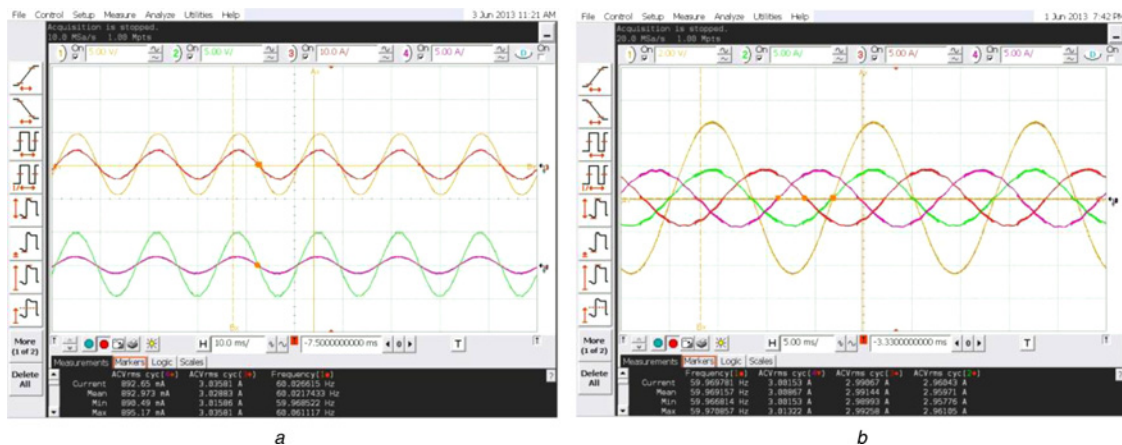
Fig. 15 *Feeding power to local load and grid*

a Voltages at the output capacitor and grid together with the local load current and the injected grid current considering phase 'a'. Green (below grey): voltage at inverters'output and yellow (upper grey): grid voltage. Time: 10 ms/div
b Active power injection to the grid. Voltage at phase 'a' (yellow (bigger grey)) together with currents over phases 'a', 'b' and 'c'. Time: 5 ms/div
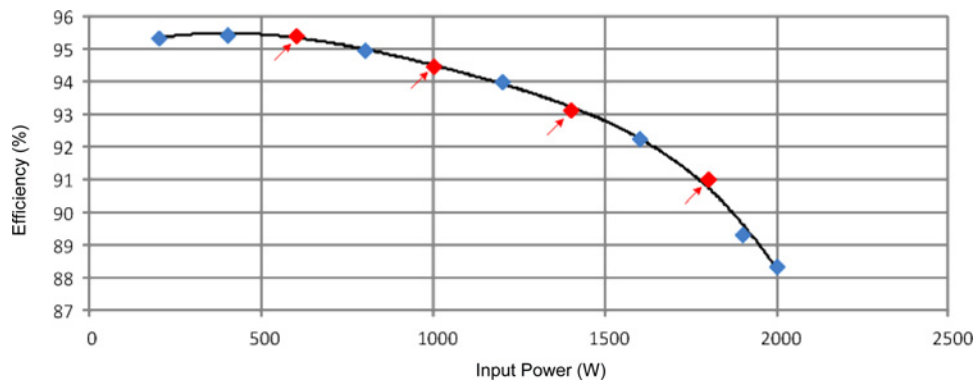
Fig. 16 *Experimental efficiency power curve, measured with Fluke 435II system*

attractive. To complement this discussion, it is presented the inverter efficiency curve in Fig. 16 that shows that this inverter is interesting for power levels in the range of 500–1500 W. The efficiency values were measured using Fluke 435 II system. The instrument is connected to all phases of the three-phase circuit. The three-phase voltages (phases A, B and C) were measured and the three-phase currents were also measured as positive when injected to the grid.

8   Conclusions

This paper has presented the integrated tri-state three-phase buck–boost inverter with special features as independent input to output control, modified SVM and $dq0$ control for both stand-alone and grid-connected modes, considering solar/PV applications. The independent input to output controls make this converter very attractive for interfacing renewable energy sources once the MPPT and output grid current injection can be controlled with high degree of freedom. The experimental results demonstrated high-quality waveforms for both stand-alone and grid-tied power injections. Moreover, the experimental evaluations proved that it is possible to control independently the input and output of the converter, with proper modulation and control of D_1 and D_2 duty cycles, demonstrating the potential and the feasibility of the application. Finally, it is important to observe that there are no power electrolytic capacitors in this integrated inverter, which results in a remarkable advantage for the working life of the structure, and it is the first time in the literature that this inverter is used to inject power into the grid.

9   References

1 Spagnuolo, G., Petrone, G., Araujo, S.V., *et al.*: 'Renewable energy operation and conversion schemes', *IEEE Trans. Ind. Electron.*, 2010, **4**, (1), pp. 38–51
2 Liserre, M., Sauter, T., Hung, Y.J.: 'Future energy systems – integrating renewable energy sources into the smart power grid through industrial electronics', *IEEE Trans. Ind. Electron.*, 2010, **4**, (1), pp. 18–37
3 De Brito, M.A.G., Galotto, L.Jr., Sampaio, L.P., Melo, G.A., Canesin, C.A.: 'Main maximum power point tracking strategies intended for photovoltaics'. Brazilian Power Electronics Conf. (COBEP), 2011, pp. 524–530
4 Esram, T., Chapman, P.L.: 'Comparison of photovoltaic array maximum power point tracking techniques', *IEEE Trans. Energy Convers.*, 2007, **22**, (2), pp. 439–449
5 De Brito, M.A.G., Sampaio, L.P., Galotto, L.Jr., Canesin, C.A.: 'Evaluation of the main MPPT techniques for photovoltaic applications', *IEEE Trans. Ind. Electron.*, 2013, **60**, pp. 1156–1167
6 Viswanathan, K., Oruganti, R., Srinivasan, D.: 'A novel tri-state boost converter with fast dynamics', *IEEE Trans. Power Electron.*, 2002, **17**, (5), pp. 677–683
7 Loh, P.C., Blaabjerg, F., Wong, C.P., Tan, P.C.: 'Tri-state current source inverter with improved dynamic performance', *IEEE Trans. Power Electron.*, 2008, **23**, (4), pp. 1631–1640
8 Sable, D.M., Cho, B.H., Ridley, R.B.: 'Use of leading-edge modulation to transform boost and flyback converters into minimum-phase-zero systems', *IEEE Trans. Power Electron.*, 1991, **6**, (4), pp. 704–711
9 Wu, W.C., Bass, R.M., Yeargan, J.R.: 'Eliminating the effects of right-half plane zero in fixed frequency boost converters'. IEEE PESC'98, 1998, vol. 1, pp. 362–366
10 De Brito, M.A.G., Sampaio, L.P., Galotto Jr., L., Canesin, C.A.: 'Tri-state single-phase integrated inverters with input to output power decoupling control'.

Int. Symp. on Power Electronics, Electrical Drives, Automation and Motion (SPEEDAM), 2012, pp. 1–6
11 Zhou, K., Wang, D.: 'Relationship between space-vector modulation and three-phase carrier-based PWM: a comprehensive analysis', *IEEE Trans. Ind. Electron.*, 2002, **49**, (1), pp. 186–196
12 Ziogas, P.D., Moran, L., Joos, G., Vincenti, D.A.: 'Refined PWM scheme for voltage and current source converter'. IEEE PESC'90, 1990, pp. 977–983
13 Brocker, H.W., Skudenly, H.C., Stanke, G.: 'Analysis and realization of a pulse width modulator based on the voltage space vectors'. IEEE-IAS Annual Meeting, 1986, pp. 244–251
14 Zaimeddine, R., Undeland, T.: 'DTC control schemes for induction motor fed by three-level NPC-VSI using space vector modulation'. Int. Symp. on Power Electronics, Electrical Drives, Automation and Motion (SPEEDAM), 2010, pp. 966–971
15 Colli, D.V., Cancelliere, P., Marignetti, F., DI Stefano, R.: 'Voltage control of current source inverters', *IEEE Trans. Energy Convers.*, 2006, **21**, (2), pp. 451–458
16 Liserre, M., Dell'aquila, A., Blaabjerg, F.: 'An overview of three-phase voltage source active rectifiers interfacing the utility'. IEEE PowerTech Conf., Bologna, Italy, 2003, pp. 1–8
17 Bolognani, S., Zigliotto, M.: 'A space-vector approach to the analysis and design of three-phase current controllers'. IEEE Int. Symp. on Industrial Electronics, 2002, pp. 645–650

10   Appendix 1

For the obtainment of the theoretical curves of Section 4 (Fig. 5), they were used (12)–(16) for the tri-state inverter and (17)–(22) for the conventional one, where the sketch of the main current waveforms can be observed through Figs. 17–19. Equation (23) is used to calculate conduction power losses considering the insulated gate bipolar transistor (IGBT) switch and (24) is used when considering the power MOSFET. Finally, (25) is considered
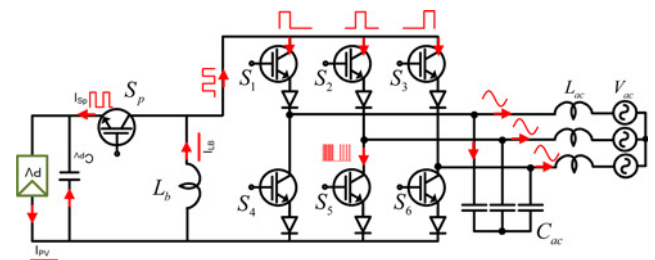

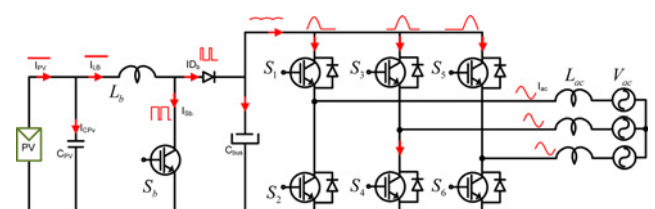**Fig. 17** *Sketch of the main current waveforms for the tri-state inverter*

Fig. 18 *Sketch of the main current waveforms for the conventional solution*
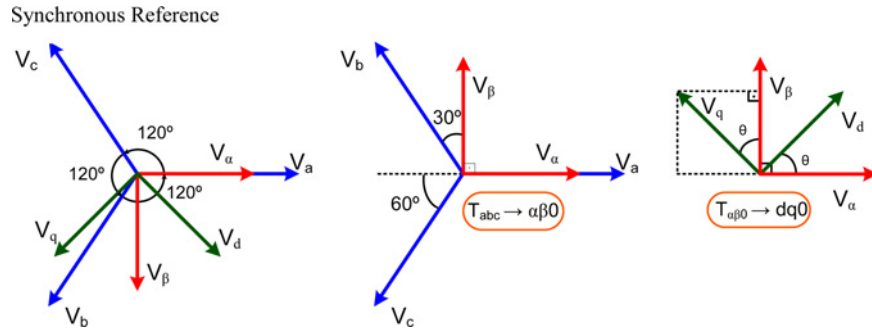
Fig. 19 *Obtainment of Matrix T*

when calculating the switching losses

$$IS_1\text{avg\_}T = \frac{1}{T}\int_0^{(1-D_1).T} I_{LB}.dt = I_{LB}.(1-D_1) \qquad (12)$$

$$IS_1\text{avg\_}f_{\text{rede}} = \frac{1}{2\pi}\int_0^{2\pi/3} I_{LB}.(1-D_1).d(\omega t) = \frac{I_{LB}.(1-D_1)}{3} \quad (13)$$

$$IS_1\text{rms\_}T = \sqrt{\frac{1}{T}\int_0^{(1-D_1).T} I_{LB}^2.dt} = I_{LB}.\sqrt{(1-D_1)} \qquad (14)$$

$$IS_1\text{rms\_frede} = \sqrt{\frac{1}{2\pi}\int_0^{2\pi/3}\left(\sqrt{I_{LB}.(1-D_1)}\right)^2.d(\omega t)}$$
$$= \frac{I_{LB}.\sqrt{(1-D_1)}}{\sqrt{3}} \qquad (15)$$

$$IS_p\text{avg} = \frac{1}{T}\int_0^{(D_1).T} I_{LB}.dt = I_{LB}.D_1 \qquad (16)$$

$$IS_b\text{avg} = I_{LB}.D \qquad (17)$$

$$ID_b\text{avg} = I_{LB}.(1-D) \qquad (18)$$

$$IS_1\text{avg} = \frac{Iac_{\text{pico}}}{\pi} \qquad (19)$$

$$IS_b\text{rms} = I_{LB}.\sqrt{D} \qquad (20)$$

$$ID_b\text{avg} = I_{LB}.\sqrt{1-D} \qquad (21)$$

$$IS_1\text{rms} = \frac{Iac_{\text{pico}}}{2} \qquad (22)$$

$$P_{\text{Con\_MOSFET}} = R_{\text{dson}}.IS_{\text{rms}}^2 \qquad (23)$$

$$P_{\text{Con\_IGBT}} = V_{\text{ce}}.IS_{\text{avg}} \qquad (24)$$

$$P_{\text{sw}} = \frac{fs}{2}\left(t_{\text{on}} + to_{\text{ff}}\right)V_{\text{max}}.I_{\text{max}} \qquad (25)$$

11 Appendix 2

Steps for the obtainment of matrix *T*, Fig (19), transformation from *abc* to *qd*0, considering synchronous reference

$$\begin{bmatrix} V_\alpha \\ V_\beta \\ V_0 \end{bmatrix} = \frac{2}{3}\begin{bmatrix} 1 & -1/2 & -1/2 \\ 0 & \sqrt{3}/2 & -\sqrt{3}/2 \\ 1/2 & 1/2 & 1/2 \end{bmatrix}\begin{bmatrix} V_a \\ V_b \\ V_c \end{bmatrix} \qquad (26)$$

$$\begin{bmatrix} V_d \\ V_q \\ V_0 \end{bmatrix} = \begin{bmatrix} \cos\theta & \text{sen}\,\theta & 0 \\ -\text{sen}\,\theta & \cos\theta & 0 \\ 0 & 0 & 1 \end{bmatrix}\begin{bmatrix} V_\alpha \\ V_\beta \\ V_c \end{bmatrix} \qquad (27)$$

$$T = \frac{2}{3}\begin{bmatrix} \cos\theta & \cos(\theta-120°) & \cos(\theta+120°) \\ -\text{sen}\,\theta & -\text{sen}(\theta-120°) & \text{sen}(\theta+120°) \\ 1/2 & 1/2 & 1/2 \end{bmatrix} \qquad (28)$$